Title

Effect of hydration on morphology of thin phosphonate block copolymer electrolyte membranes studied by electron tomography

Journal

Polymer Engineering & Science, 61(4)

ISSN

0032-3888

Authors

Jiang, Xi
Sun, Jing
Zuckermann, Ronald N
et al.

Publication Date

2021-04-01

DOI

10.1002/pen.25646

Peer reviewed

Effect of hydration on morphology of thin phosphonate block copolymer electrolyte membranes studied by electron tomography

Xi Jiang [1], Jing Sun[4], Ronald N. Zuckermann[2], Nitash P. Balsara[1,3] **

1. Materials Sciences Division, Lawrence Berkeley National Laboratory, Berkeley, CA 94720, USA

2. Molecular Foundry, Lawrence Berkeley National Laboratory, Berkeley, CA 94720, USA

3. Department of Chemical and Biomolecular Engineering, University of California, Berkeley, CA 94720, USA

4. Key Laboratory of Biobased Polymer Materials, Shandong Provincial Education Department, School of Polymer Science and Engineering, Qingdao University of Science and Technology, Qingdao 266042, China

*Corresponding author: xijiang@lbl.gov; nbalsara@berkeley.edu

Submission to Polymer Engineering & Science

Abstract (200 words max)

The morphological changes of phosphonate polypeptoid electrolyte membranes, poly-*N*-(2-ethyl)hexylglycine-*block*-poly-*N*-phosphonomethylglycine (pNeh$_m$-*b*-pNpm$_n$), in hydrated and dry states were characterized by cryogenic transmission electron microscopy (cryo-TEM) and cryogenic electron tomography (cryo-ET). The analysis of 3D tomograms revealed that the pNeh$_9$-*b*-pNpm$_9$ thin films absorbed a large amount of water, resulting in the formation of membranes that were nearly flat and giant multicompartment vesicles dispersed in the water phase. A simple lamellar phase appeared when the films were dried. In contrast, pNeh$_{18}$-*b*-pNpm$_{18}$ thin films absorbed little water and formed small highly curved unilamellar and multilamellar vesicles. Water was located mainly outside the closely-packed vesicles. When water was removed by drying, the walls of adjacent vesicles collapsed to form honeycomb-like capsules. The changes in domain size reflected changes in chain conformations. The pNpm$_9$ blocks were saturated by water and fully extended, while pNpm$_{18}$ blocks were neither saturated by water nor fully extended. In addition, the thicknesses of hydrophobic blocks in the hydrated films of both pNeh$_9$-*b*-pNpm$_9$ and pNeh$_{18}$-*b*-pNpm$_{18}$ were smaller than those in the dry films, reflecting an increase of the average distance between the neighboring junctions of polypeptoid molecules.

keywords (3-7 keywords)

polypeptoid, polymer electrolyte membrane, cryogenic, low-dose, transmission electron microscopy, electron tomography

Introduction

Polymer electrolyte membranes have attracted considerable attention in recent years due to their application in fuel cells,[1,2] lithium-ion batteries,[3,4] and artificial photosynthesis.[5] These polymers generally comprise conductive microphases that enable ion transport and rigid insulating microphases that provide the membrane with the mechanical properties necessary for large-scale manufacturing and operation in devices. Hydration of polymer electrolyte membranes is important for applications related to proton transport (fuel cells, artificial photosynthesis, etc.). Hydrated membranes are also important in the field of drug delivery due to the spontaneous formation of structures capable of carrying therapeutic agents such as micelles and vesicles.[6-10] Block copolymers consisting of hydrophobic blocks and hydrophilic blocks serve as model systems for studying the effect of hydration on nanoscale morphology.

The phase behavior of hydrated block copolymers (in bulk samples) has been studied extensively by scattering methods (X-ray and neutron).[4,11-15] Scattering data reveals the statistically averaged global morphology of the sample. Probing the microphase separation of individual nanodomains can only be achieved by direct imaging methods such as transmission electron microscopy (TEM) and atomic force microscopy (AFM).[16,17] In contrast to surface information provided by AFM, TEM enables investigation of the interior structures of thin specimens. However, polymers are easily damaged by electron beam exposure, and minimizing the damage caused by the electron beam radiation is essential. This is enabled by low-dose cryogenic transmission electron microscopy (cryo-TEM). The effect of radiation damage is minimized when the specimen is cooled to cryogenic temperatures leading to the preservation of

high spatial frequency information.[18-22] In addition, vitrification results in the preservation of the natural state of the specimen, such as self-assembled soft materials in solution. [23-30]

Nafion, the most intensively studied polymer electrolyte membrane, is a random copolymer comprised of hydrophobic semi-crystalline tetrafluoroethylene backbones and hydrophilic perfluoroether side chains with sulfonic acid termini. In the dry state, the sulfonic acid ionic clusters are sequestered in the hydrophobic matrix, while percolating channels of hydrated sulfonic acid form within the hydrophobic matrix in the hydrated state. The structure of Nafion has mainly be determined by interpreting the X-ray and neutron scattering patterns. The patterns were fitted based on the interpretation of amplitude information without phase information in Fourier space. There are, therefore, numerous models for the morphology that have been proposed. [15,31-33] To facilitate the accurate structural study, AFM,[34,35] X-ray ptychography, [36] and TEM[37,38] have been used for direct two-dimensional (2-D) imaging of hydrated and dry Nafion at the nanoscale. In addition, the 3D morphologies of hydrated and dry Nafion were studied by X-ray tomography,[39-41] electron tomography (ET),[42,43] and cryogenic transmission electron tomography (cryo-ET)[44] at various length scales from micrometer to nanoscale in position space. These analyses of 3D reconstructed Nafion, in the hydrated bulk and thin film, quantitatively revealed the effect of water on the morphological changes and the spatial distribution of water channels.

Morphological studies of polymer electrolyte membranes are facilitated by the presence of well-defined hydrophilic and hydrophobic blocks. TEM and scanning transmission electron microscopy (STEM) have been widely used to directly image the morphology and distributions of acid groups in dry thin films of sulfonated ionomers. [45-52] However, the analyses of 2-D projection were limited by overlapped features in the thin film, (thickness is much larger than

acid group size), and electron beam damage.[37,53] Low-dose imaging and STEM tomography 3D reconstructions enabled the quantitative characterization of the location and size distribution of sulfur-rich clusters in a free-standing dry polystyrene sulfonate-*b*-polymethylbutylene (PSS-*b*-PMB) thin film. [54] The characterization of hydrated films requires the preservation of hydration. Cryo-ET has been widely used to characterize the internal structures of self-assembled block copolymers in solution.[45,55-58] More recently, cryo-ET was applied to study the presence of water channels in the hydrated membranes comprised of sulfonated block copolymers.[59] 3D reconstructed tomograms in position space revealed the presence of a distinct morphology of a polymer electrolyte membrane in the hydrated state as compared to that in the dry state.

As compared to the sulfonated block copolymer electrolytes, phosphonate block copolymers are attractive systems due to the efficient proton transport under low water uptake conditions,[60] and higher chemical and thermal stability.[61] We previously reported the synthesis and characterization of a family of well-defined phosphonate polypeptoid diblock copolymers: poly-N-(2-ethyl)hexylglycine-block-poly-N-phosphonomethylglycine (pNeh-*b*-pNpm) with volume fractions of pNpm (ϕ_{Npm}) at 0.44 and dispersity ($Đ$) $\leq$ 1.0003 using an iterative solid-phase method.[62] Microphase separation in the hydrated bulk film results in the formation of pNpm-rich domains that conduct protons. The purpose of this study is to reveal the nature of microphase separation in the hydrated pNeh-*b*-pNpm thin films at the nanoscale. We studied two symmetric pNeh-*b*-pNpm block copolymers with different chain lengths. We focus on the morphology of hydrated and dried (after water vapor annealing) thin films characterized by cryo-ET. In the hydrated state, the reconstructed tomograms demonstrate that the $pNeh_9$-*b*-$pNpm_9$ molecules (the smaller chain length sample) absorb a large amount of water, resulting in the formation of membranes that are nearly flat and giant multicompartment vesicles dispersed in the

water phase. In contrast, $pNeh_{18}$-*b*-$pNpm_{18}$ molecules self-assembled into small closely-packed unilamellar and multilamellar vesicles surrounded by narrow water channels. When the hydrated films are dried, the two pNeh-*b*-pNpm thin films exhibit different morphologies: $pNeh_9$-*b*-$pNpm_9$ exhibits a lamellar morphology, while $pNeh_{18}$-*b*-$pNpm_{18}$ forms honeycomb-like polygonal capsules. Quantitative analysis of the tomograms indicates that drying results in a decrease in the hydrophilic domain size and an increase in the hydrophobic domain size in both polymers.

Experimental section

Polypeptoids synthesis

Two sequence-defined amphiphilic polypeptoid block copolymers, poly-*N*-(2-ethyl)hexylglycine-*block*-poly-*N*-phosphonomethylglycine ($pNeh_m$-*b*-$pNpm_n$), were synthesized as described in our previous work. [62] The chemical structure of the copolymer is shown in Figure 1A. The characteristics of the copolymers (*m, n*, molecule weight and polydispersity) are given in Table 1. The polypeptoids in Table 1 have a fixed block ratio (the ratio m/n=*1*) and a fixed volume fraction (ϕ_{Npm} = 0.44), as depicted in Figure 1B. Amphiphilic polypeptoids were dissolved in a tetrahydrofuran (THF) /water mixture (1:1 v/v). The concentration of the solutions was 0.1 mg/mL.

Preparation of thin films

Thin films were prepared by drop casting five microliter droplets on the gold grids covered by lacey carbon supporting films with pre-deposited 10 nm diameter gold colloid nanoparticles (TedPella, Inc). After the evaporation of the solvent, the grids with the as-cast thin films were annealed in the humidity chamber of a Vitrobot (FEI Inc.) at 20 °C in air with 100% relative humidity (RH) for two hours. The frozen hydrated films were prepared by plunging the grids into liquid ethane in a Vitrobot and then stored in liquid nitrogen for cryo-transfer. The dry films

(after water vapor annealing) were prepared by partially dehydrating the annealed films in air (35% humidity) and then fully under ultrahigh vacuum (lower than 10^{-7} Torr) in the transmission electron microscope column.

Cryo-TEM and cryo-ET characterizations

The grids covered by the as-cast dry thin films and the grids covered by dry (after annealing) thin films were loaded at room temperature and then cooled down to liquid nitrogen temperature in the microscope column. The grids covered by the frozen hydrated thin films were cryo-transferred in to the microscope under the protection of liquid nitrogen to preserve the natural state. Micrographs and tomograms of the as-cast dry thin film, the frozen hydrated thin film and the dry thin film (after water vapor annealing) were collected using a JEOL-3200FSC transmission electron microscope (JEOL Inc. Japan) at 300 KeV with the energy filter slit width at 30 eV at -175°C. Micrographs were recorded at 20K magnification on the JEOL-3200FSC by a K2 direct electron detector in counting mode with 10 frames in each dose fractionation movie. The dose fractionation movies were aligned and summed using Motioncorr2.[63] The accumulated dose used to obtain the micrographs and the tilt series were ~ 20 $e/Å^2$ and ~ 80 $e/Å^2$, respectively. Single tilt series for tomography were collected in the angle range of −60° to 60° with the increment of 4 degrees for each tilt series. Alignment, CTF correction and 3D reconstruction were carried out using the IMOD tomographic reconstruction software package.[64] The reconstructed tomograms were denoised using nonlinear anisotropic diffusion (NAD) filter, segmented and colored in IMOD.[64] It is important to note that the thicknesses of hydrated and dry films were measured based on the tomograms collected from different locations on the different grids so that they cannot be compared directly to calculate water uptake. All thin films used in this study were not stained.

Results and discussion

Figure 2A shows a cryo-TEM image of an as-cast pNeh$_9$-*b*-pNpm$_9$ film. This image is featureless. Figure 2B shows a cryo-TEM image of the same sample in the hydrated state after it has been annealed in water vapor for two hours. The sample exhibits a lamellar morphology; some lamellae are curved, but the radius of curvature is much greater than the thickness of the lamellae. The hydrated pNeh$_9$-*b*-pNpm$_9$ film was dried and imaged, and the result is shown in Figure 2C. The lamellar morphology in the dry film is similar to that in the hydrated state. However, the domain sizes are different and the contrast is weaker. The dark regions in all the images in this paper represent the electron dense phosphorus-rich pNpm microphase. In many figures, however, the distinction between the pNeh and pNpm phases is unclear, as is the case in Figure 2 where the dark bands represent the edges of polymeric membranes. Figure 2D shows a cryo-TEM image of an as-cast dry pNeh$_{18}$-*b*-pNpm$_{18}$ film. While weak microphase separation is seen in this film, there are no obvious signatures of a well-defined morphology. Figure 2E shows a cryo-TEM image of the same sample in the hydrated state after it has been annealed in water vapor. This sample also exhibits lamellar morphology but the lamella in pNeh$_{18}$-*b*-pNpm$_{18}$ are more highly curved and less well-defined than those in pNeh$_9$-*b*-pNpm$_9$. Drying the hydrated pNeh$_{18}$-*b*-pNpm$_{18}$ film results in the formation of thin dark lines that outline a honeycomb-like morphology. It is evident that the morphologies of dry films are affected by annealing history; compare Figures 2A and 2C, and Figures 2D and 2F.

The low signal-to-noise ratio (SNR) in the low-dose micrographs in Figure 2 hinders accurate characterization of the morphologies. In particular, the clarity of micrographs decreases when the film thicknesses increase due to hydration. Interpretation of morphologies based on 2D

projections sometimes lead to controversy, and discrepancies are found between imaging and scattering characterization.[14,15,31,44,65,66] It is therefore important to examine the 3D morphologies of our polypeptoid thin films in both hydrated and dry states.

Cryogenic electron tomography was used to obtain the morphologies of microphase separated structures after water vapor annealing in the hydrated films and in films that were dried after hydration. In the discussion below, we only focus on the dried films obtained after hydration, not the dry as-cast films. Figures 3A and B show the 3D tomographic reconstructions of the hydrated thin films of $pNeh_9$-*b*-$pNpm_9$. Supporting movie 1 shows all *x*-*y* plane slices in the tomogram. Figure 3A shows a slice perpendicular to the projection direction (*z* axis) of the reconstructed tomogram. It displays horizontal cross-section (*x*-*y* plane) through the hydrated thin film. It is evident that the hydrated $pNeh_9$-*b*-$pNpm_9$ thin film exhibits the presence of a wide variety of morphologies. The dark bands seen throughout the slice represent membranes obtained by the self-assembly of $pNeh_9$-*b*-$pNpm_9$ molecules; we posit that these bands indicate the locations of both hydrophilic and hydrophobic blocks. They primarily represent the walls of vesicles. We find unilamellar and multilamellar vesicles. In addition, we observe multicompartment structures where small vesicles are in enclosed in the larger ones. The clarity with which morphologies can be identified in the 3D tomogram in Figure 3A is significantly better than the 2D projection of the same sample shown in Figure 2B obtained by cryo-TEM. This is because interference from structures below and above the *x*-*y* plane shown in Figure 3A has been eliminated. Three boxes numbered from 1 to 3 in Figure 3A have been chosen for further study. The 3D structure of the vesicle contained in box 1 is shown in Figure $3B_1$. The location of the dark regions representing the two membranes of the vesicles in three-dimensions are shown by mesh rendering in two colors (half vesicles are shown for clarity). Each vesicle

membrane is comprised of a hydrophobic pNeh core and hydrophilic pNpm brushes.[67] The space between the two vesicle membranes must be filled with water (the interior of the small vesicle must also contain water). Figure $3B_1$ gives an indication of the thickness of the frozen hydrated thin film; the vesicle in box 1, which has a diameter of about 120 nm, is entirely contained within the film. The 3D structure of the membranes in box 2 is shown in Figure $3B_2$. These membranes are essentially perpendicular to the *x*-*y* plane and are reminiscent of the classical lamellar phase found in block copolymers.[68,69] The data in Figures 3A and B do not quantitatively reveal the nature of microphase separation within the $pNeh_9$-*b*-$pNpm_9$ membrane. This discussion will be presented shortly using the box labeled 3 in Figure 3A.

A thin film $pNeh_9$-*b*-$pNpm_9$ was subjected to the same water annealing protocol described above followed by drying as described in the Experimental Section. Figures 3C and D show the 3D tomographic reconstructions of the dried film. (See supporting movie 2 for details.) Drying a $pNeh_9$-*b*-$pNpm_9$ film after hydration results in the formation of deformed membranes and broken vesicles. The dark lines seen throughout the slice are distinctly thinner than the dark bands seen in the Figure 3A. Stacks of lamella oriented perpendicular to the *x*-*y* plane are evident in many locations. The bright regions in these stacks represent the locations of the hydrophobic pNeh blocks. The 3D structures associated with boxes 1 and 2 in Figure 3C are shown in Figure 3D. Figure $3D_1$ shows a multilamellar vesicle that was broken by the drying process. Figure $3D_2$ shows a stack of parallel lamellae that are analogous to the stack shown in Figure $3B_2$. The data in box labeled 3 will be used to quantitatively determine the morphology of dry $pNeh_9$-*b*-$pNpm_9$ film in the discussion below.

The 3D tomographic reconstruction of the hydrated thin film of $pNeh_{18}$-*b*-$pNpm_{18}$ is shown in Figure 4A. (Supporting movie 3 shows all *x*-*y* plane slices in the tomogram.) The

coexistence of multilamellar and multicompartment vesicles is clearly seen. It is noteworthy that the density of vesicles in the hydrated $pNeh_{18}$-*b*-$pNpm_{18}$ thin film is much higher than that in the hydrated $pNeh_9$-*b*-$pNpm_9$ thin film. The data in the three boxes numbered from 1 to 3 are indicated by dashed white lines. They will be used for 3D visualization and further discussion. As was the case in Figure 3, the 3D membrane morphology is visualized by mesh rendering. The 3D visualized vesicles (half vesicles are shown for clarity) in box 1 and 2 are shown in Figures $4B_1$ and B_2. Multilamellar vesicles with three layers and two layers are indicated by different colors in box 1 and box 2, respectively. The data in box 3 will be used to quantitatively determine the morphology of hydrated $pNeh_{18}$-*b*-$pNpm_{18}$ film shortly.

A slice from the tomogram of a dry $pNeh_{18}$-*b*-$pNpm_{18}$ thin film (after annealing in water vapor) is shown in Figure 4C. (See supporting movies 4 for details.) It is evident that the drying process causes a significant rearrangement of hydrated vesicles. In some regions, we see relatively large multilamellar capsules (dry vesicles) – see box 1 in Figure 4C. In other regions, we see coalesced unilamellar capsules with a polygonal shape – see box 2. Both kinds of capsules are curved in the *z* direction as shown in the 3D visualizations in Figures $4D_1$ and D_2. However, the tops of the capsules are flat. In Figure 4C, careful examination of the regions within each capsule reveals two different shades of grey: a light grey band that surrounds the black lines representing the membrane and a dark grey interior. The dark grey interior is the projection of the flat top of each capsule. The light grey band represents the extent of capsule curvature in the *z* direction. This is clarified in Figure 4D.

The thicknesses of the films were measured in the 3D reconstructed tomograms. (See Figure S1 in SI.) Although the thin films of two polypeptoid block copolymers were prepared by drop casting the same amount of solution with the same concentration (0.1mg/mL) on the lacey

carbon supporting films, the resulting film thicknesses were very different. The thickness of hydrated $pNeh_9$-*b*-$pNpm_9$ film was uniform and about 240 nm. The hydrated $pNeh_{18}$-*b*-$pNpm_{18}$ film was also uniform with a thickness of about 100 nm. This difference, reflecting different levels of water uptake, leads to significant differences in the thickness of the dry films. The dry $pNeh_9$-*b*-$pNpm_9$ film has a uniform thickness of about 130 nm. The thickness of dry $pNeh_{18}$-*b*-$pNpm_{18}$ film is not uniform, ranging from 30 to 70 nm. The thickness of the film above box 1 in Figure 4 is about 70 nm while that of box 2 is about 30 nm.

It is common to create large vesicles by rehydrating dry films of lipids.[70,71] Our results show that $pNeh_9$-*b*-$pNpm_9$ is better suited for this than $pNeh_{18}$-*b*-$pNpm_{18}$. $pNeh_9$-*b*-$pNpm_9$ absorbs more water and readily forms large loosely-packed vesicles in thin films while $pNeh_{18}$-*b*-$pNpm_{18}$ absorbs less water and forms small closely-packed vesicles.

In the hydrated state, membranes shown in Figures 3 and 4 must exhibit microphase separation with dry hydrophobic pNeh cores and hydrophilic pNpm brushes extending outward from the cores.[72,73] This aspect of the morphology is, however, not evident in the images discussed thus far. Figure 5 shows the horizontal slices (*x*-*y* plane in the top panel) and the corresponding perpendicular slices (*y*-*z* plane as indicated by the dashed red lines in the bottom panel) of small portions in the hydrated and dry films as indicated by boxes 3 in Figures 3 and 4. Two-dimensional Fourier transforms of the slices (shown as inset) and their one-dimensional (1-D) radial profiles (rotational averaged Fourier transforms) of the *x*-*y* plane slices are shown in the right panel in each figure. The slices in *x*-*y* plane and *y*-*z* plane in Figure 5A show the membrane morphology in the hydrated $pNeh_9$-b-$pNpm_9$ thin film. The dark bands represent the phosphorus-rich pNpm brushes. The thin grey bands between adjacent pNpm brushes represent the pNeh hydrophobic cores. The broad grey bands represent absorbed water. The 1-D profile of the FFT

in the left panel shows two major peaks. The first peak occurs at 15 nm and the second peak occurs at 7.5 nm.

The slices in Figure 5B show the lamellae vertically arranged in the dried $pNeh_9$-b-$pNpm_9$ thin film after water vapor annealing. Slices in both *x*-*y* and *y*-*z* planes indicate the presence of a well-ordered lamellar morphology. The dark regions represent the phosphorus-rich pNpm blocks, while the grey regions represent the hydrophobic pNeh blocks. The 1-D profile of the FFT in the left panel shows two major peaks. The first peak occurs at 7.5 nm and the second peak occurs at 3.7 nm.

Figure 5C shows the membrane structure of vesicles in the hydrated $pNeh_{18}$-b-$pNpm_{18}$ thin film. In the *x*-*y* plane, we see two bilayer vesicles, one has a capsule-like cross-section and the other is circular. Similar to that in the hydrated $pNeh_9$-b-$pNpm_9$ thin film, the dark regions are attributed to the phosphorus-rich pNpm brushes. There are two grey regions within each vesicle. They represent the hydrophobic pNeh cores. The space between the vesicles has different length scales in different regions in the slice. We posit that absorbed water resides in these regions. Two peaks are observed in the 1-D FFT profile in Figure 5C. The first peak occurs at 7.8 nm and the second peak occurs at 5.0 nm.

Figure 5D shows a magnified view of the morphology of the dried $pNeh_{18}$-b-$pNpm_{18}$ thin film. We see three different capsules: a rectangular capsule and two polygonal capsules. The rectangular capsule has a 7.0 nm wide light grey interior. The dark outline of the capsule represents the pNpm blocks while the light grey interior represents the pNeh blocks. This capsule represents a dried unilamellar vesicle. The polygonal capsules have a 7.0 nm wide outer light grey band and a darker grey interior. The *y*-*z* plane slice shown in Figure 5D shows a complex onion-like morphology in the interior of capsule. The slices only allow for the determinations of

the location of the pNpm blocks that outline the capsule; the exact nature of the microphase separation in the interior of capsule is beyond the resolution of our approach. Two peaks are observed in the 1-D FFT profile in Figure 5D. The first peak occurs at 10.5 nm and the second peak occurs at 5.4 nm.

Frequency filters were applied to the images of the hydrated $pNeh_9$-b-$pNpm_9$ thin films in Figure 5A with a cutoff frequency at 0.125 nm^{-1}. Our objective was to sort out the origin of the primary and secondary peaks in FFT, as done in a previous study.[74] The low-pass filtered and high-pass filtered images are shown in Figures 6A and B, respectively. The 1-D FFT profiles with corresponding frequency ranges in the Fourier space are shown in the bottom panels in Figures 6A and B. The low-pass filtered slice in Figure 6A reveals the periodic structure with alternating polymer membrane and water layers. The high-pass filtered slice in Figure 6B shows the internal structure of the polymer membrane. The membrane structure, comprised of two dark hydrophilic pNpm bushes and a grey hydrophobic core, is evident in this Figure.

The same analysis with a cutoff frequency at 0.166 nm^{-1} was applied to the slice of the hydrated $pNeh_{18}$-*b*-$pNpm_{18}$ film shown in Figure 5C. The low-pass filtered and high-pass filtered images are shown in Figures 6D and E, respectively. In this case, both images are similar, reflecting the fact that the pNeh, pNpm and water microphases have similar dimensions. Particularly, the thickness of water microphase in $pNeh_{18}$-*b*-$pNpm_{18}$ is much smaller than that of $pNeh_9$-*b*-$pNpm_9$. The high-pass filtered image, Figure 6E, clarifies the size and geometry of the water phase that surround the vesicles.

Figures 6C shows a schematic of the morphology of the hydrated $pNeh_9$-b-$pNpm_9$ thin film. The averaged thicknesses of each domain in the schematic were measured using line

profiles across the images in Figures 6A and B. The absorbed water phase between two membranes has the thickness at 8.1 nm. The averaged thickness of membrane is 7.2 nm, comprising two hydrophilic brush layers (each is 2.4 nm thick) and a hydrophobic core (2.4 nm). The fully stretched chain length of $pNpm_9$ and $pNeh_9$ is about 2.8 nm when the chains are in *all-trans* conformation.[75,76] The measured thickness suggests that the $pNpm_9$ brushes are strongly stretched and saturated by water. Inferences regarding of the nature of $pNeh_9$ chains depend on whether the chains emanating from either side of the hydrophobic core interdigitated or not. The electron microscopy results thus cannot be used to determine chain conformations in the hydrophobic core. As shown in Figure 6F, the hydrated $pNeh_{18}$-b-$pNpm_{18}$ thin film shows different domain sizes. The averaged thickness of the membrane is 11.0 nm, comprising two hydrophilic brush layers (each is 3.3 nm thick) and a hydrophobic core (4.4 nm). The averaged thicknesses of each domain in the schematic were measured using line profiles across the images in Figures 6D and E. The fully stretched chain length of $pNpm_{18}$ is two times longer than that of Npm_9, which is about 5.6 nm when the backbones are in *all-trans* conformation. Interestingly, the measured thickness suggests the $pNpm_{18}$ and $pNeh_{18}$ chains are not as strongly stretched as $pNpm_9$ and $pNeh_9$.

The thicknesses of the different domains in the hydrated and dry films are summarized in Table 2. It is interesting to note that the thickness of hydrophobic block in the hydrated film is smaller than that in the dry film. It is perhaps not surprising to observe this change in the polypeptoid diblock copolymers. As reported by Koizumi et al.,[77] when a molecule with a small molecular weight like water is solubilized into one of the microdomains of a diblock copolymer, it causes an expansion of the average distance between the neighboring junctions of block

copolymer molecules at the interface, resulting in a decrease in the thickness of the insoluble domain.

The molecular underpinnings of our observation remain to be established. Our experiments show that the lower molecular weight pNeh9-*b*-pNpm9 sample absorbs significantly more water that the higher molecular weight pNeh18-b-pNpm18. The low polymer concentration in hydrated pNeh9-*b*-pNpm9 resulted into a morphology of loosely packed large vesicles. In contrast, the high polymer concentration in hydrated pNeh18-*b*-pNpm18 resulted into closely packed small vesicles. These two vastly different morphologies serve as the initial state for the drying process. It is therefore not surprising that the dry morphologies appear to be greatly affected by the hydrated morphologies. In the case of pNeh9-*b*-pNpm9, individual vesicles collapse and break during drying process. In the case of pNeh18-*b*-pNpm18, neighboring vesicles collapse to give honeycomb-like structures. The presence of straight lines in the micrograph of dry pNeh18-*b*-pNpm18 suggests that these membranes are more elastic than the pNeh9-*b*-pNpm9 membranes.

Conclusion

We studied the effect of hydration on the morphology of thin phosphonate electrolyte films formed by two sequence-defined amphiphilic polypeptoid block copolymers. The block ratio was identical (1:1) but the chain length (m/n) varied from 18/18 to 9/9. The analyses of 3D tomograms revealed that the $pNeh_9$-*b*-$pNpm_9$ thin films absorbed a large amount of water inside large multicompartment vesicles. The vesicle membranes were almost flat on the length scale of the membrane thickness; they were very similar to the swollen lamellar phase. It was thus not

surprising that a simple lamellar phase appeared when the films were dried. In contrast, $pNeh_{18}$-*b*-$pNpm_{18}$ thin films absorbed little water and formed small highly curved unilamellar and multilamellar vesicles. Water was located mainly outside the closely-packed vesicles. When water was removed by drying, the walls of adjacent vesicles collapsed to form onion-like capsules. The morphological change was much like collapsing bubbles to give a foam. A combination of low-dose cryo-TEM imaging and 3D tomography was essential to reveal these unique morphologies. The changes in domain size reflect changes in chain conformations. The $pNpm_9$ blocks were saturated by water and fully extended, while $pNpm_{18}$ brushes were neither saturated by water nor fully stretched. In addition, the thicknesses of hydrophobic blocks in the hydrated films of both $pNeh_9$-*b*-$pNpm_9$ and $pNeh_{18}$-*b*-$pNpm_{18}$ are smaller than those in the dry films, reflecting an increase of the average distance between the neighboring junctions of polypeptoid molecules. These findings reveal the complex nature of the relationship between the molecular structure of block copolymers and thin film morphology. We hope that our experiments will lead to a better understanding of the effect of chain length on self-assembly of amphiphilic block copolymers in thin films.

Acknowledgments

Funding for this work was provided by the Soft Matter Electron Microscopy Program (KC11BN), supported by the Office of Science, Office of Basic Energy Science, US Department of Energy, under Contract DE-AC02-05CH11231. Work at the Molecular Foundry was supported by the Office of Science, Office of Basic Energy Sciences, of the U.S. Department of Energy under Contract No. DE-AC02-05CH11231. Micrographs presented here were collected at the Donner Cryo-EM resources in Lawrence Berkeley National Laboratory. NPB

acknowledges the important role that Chris Macosko played in his education, beginning in 1988 when he was a post-doc working in the polymer program that Chris established at the University of Minnesota and through the intervening years as NPB established his independent research program. Chris has made pioneering contributions to the field of polymer science, including cryo-EM characterization.[9,10]

Corresponding Authors

* Correspondence to: xijiang@lbl.gov (X.J); nbalsara@berkeley.edu (N.P.B)

Conflict of Interest Statement

The authors declare no competing financial interest.

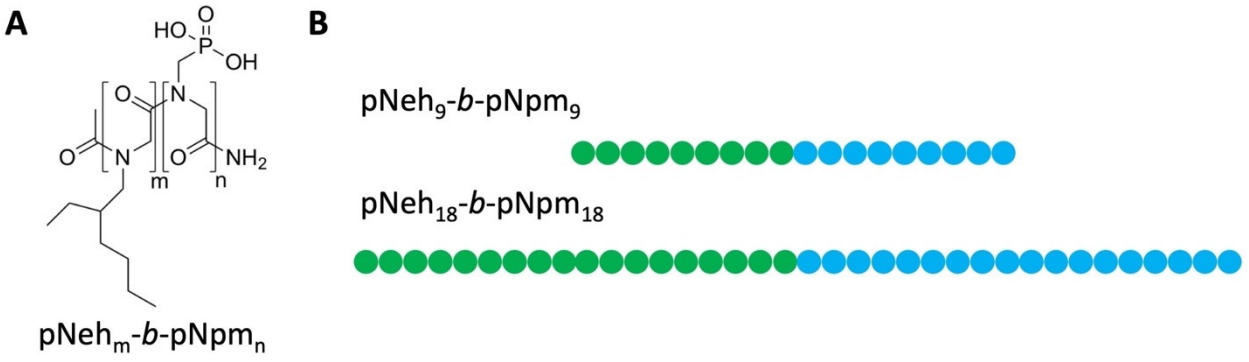

Figure 1. A. Chemical structure of amphiphilic polypeptoid block copolymer; **B.** Schematic cartoon of molecular structure represents the amphiphilic polypeptoids with different chain length but same block ratio. The green and blue spheres represent the repeating units in the hydrophobic pNeh block and the hydrophilic pNpm block, respectively.

Table 1. Characteristics of the diblock polypeptoids $pNeh_m$-*b*-$pNpm_m$

Polypeptoids	*m*	*n*	molar mass[1] (g/mol, calc/obs)	Dispersity[2]
$pNeh_9$-*b*-$pNpm_9$	9	9	2941.4/2941.4	1.0003
$pNeh_{18}$-*b*-$pNpm_{18}$	18	18	5823.8/5824.7	1.0001

[1.] Determined by electrospray ionization (ESI) mass spectrum.[62]

[2.] PDI is estimated as described by the ESI and matrix assisted laser desorption/ionization mass spectrometry (MALDI) data.[62]

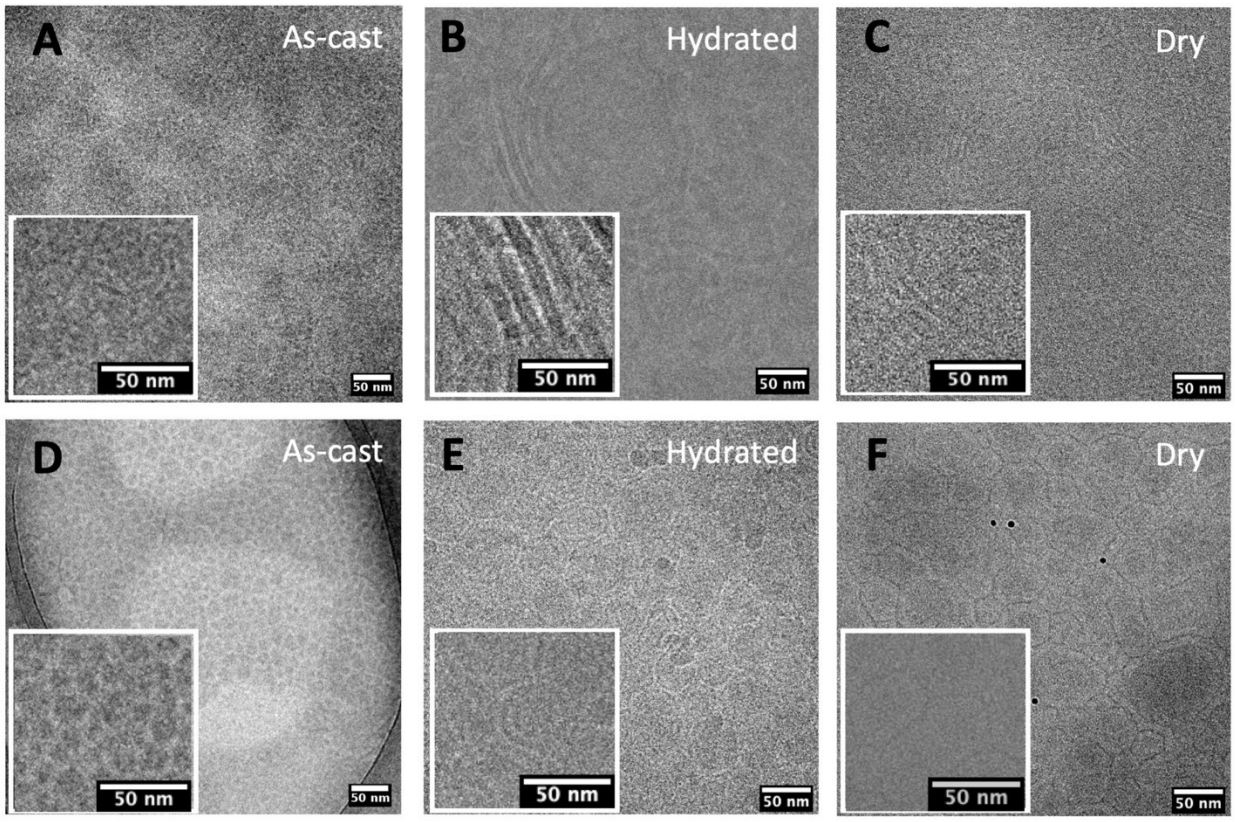

Figure 2. Low-dose bright field cryo-EM micrographs (2D projections) show the morphologies of the as-cast, the hydrated, and the dry polypeptoids thin films after annealing in water vapor, respectively. Magnified regions are shown in the boxes **A**.as-cast $pNeh_9$-*b*-$pNpm_9$ thin film, **B.** frozen hydrated $pNeh_9$-*b*-$pNpm_9$ thin film and **C.** dry $pNeh_9$-*b*-$pNpm_9$ thin film; **D**.as-cast $pNeh_{18}$-*b*-$pNpm_{18}$ thin film, **E.** frozen hydrated $pNeh_{18}$-*b*-$pNpm_{18}$ thin film and **F.** dry $pNeh_{18}$-*b*-$pNpm_{18}$ thin film;

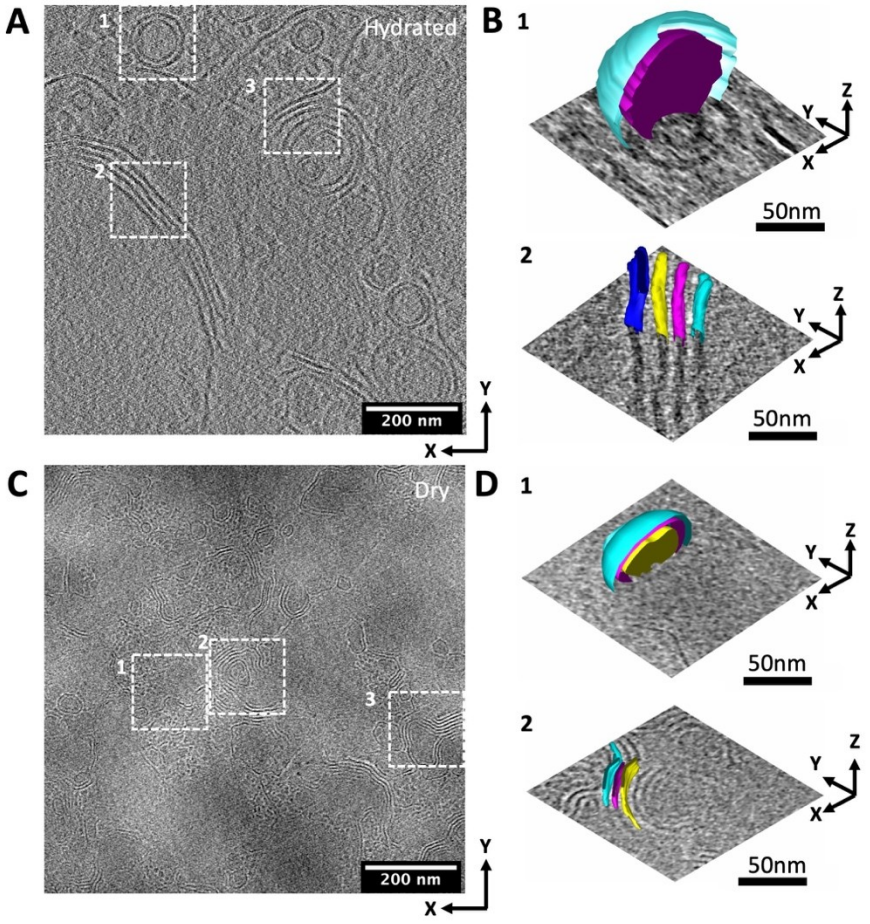

Figure 3. Slices in the tomograms show the morphological changes in the hydrated and dry $pNeh_9$-*b*-$pNpm_9$ thin films, respectively. **A**. a perpendicular slice through the tomogram of the hydrated $pNeh_9$-*b*-$pNpm_9$ thin film, **B.** 3D visualizations of two regions, 1 and 2, labeled by

dashed boxes in A. Different colors represent the spatial distributions of the central regions of the membranes using mesh rendering in iMOD. **C**. a perpendicular slice through the tomogram of the dry $pNeh_9$-*b*-$pNpm_9$ thin film, **D.** 3D visualizations of two regions, 1 and 2, labeled by dashed boxes in C. Different colors represent the spatial distributions of the central regions of the electron dense pNpm blocks using mesh rendering in iMOD. The areas indicated by box 3 are shown in Figures 5 and 6. One slice along z direction is shown in each panel. The thickness of a slice is 0.8 nm.

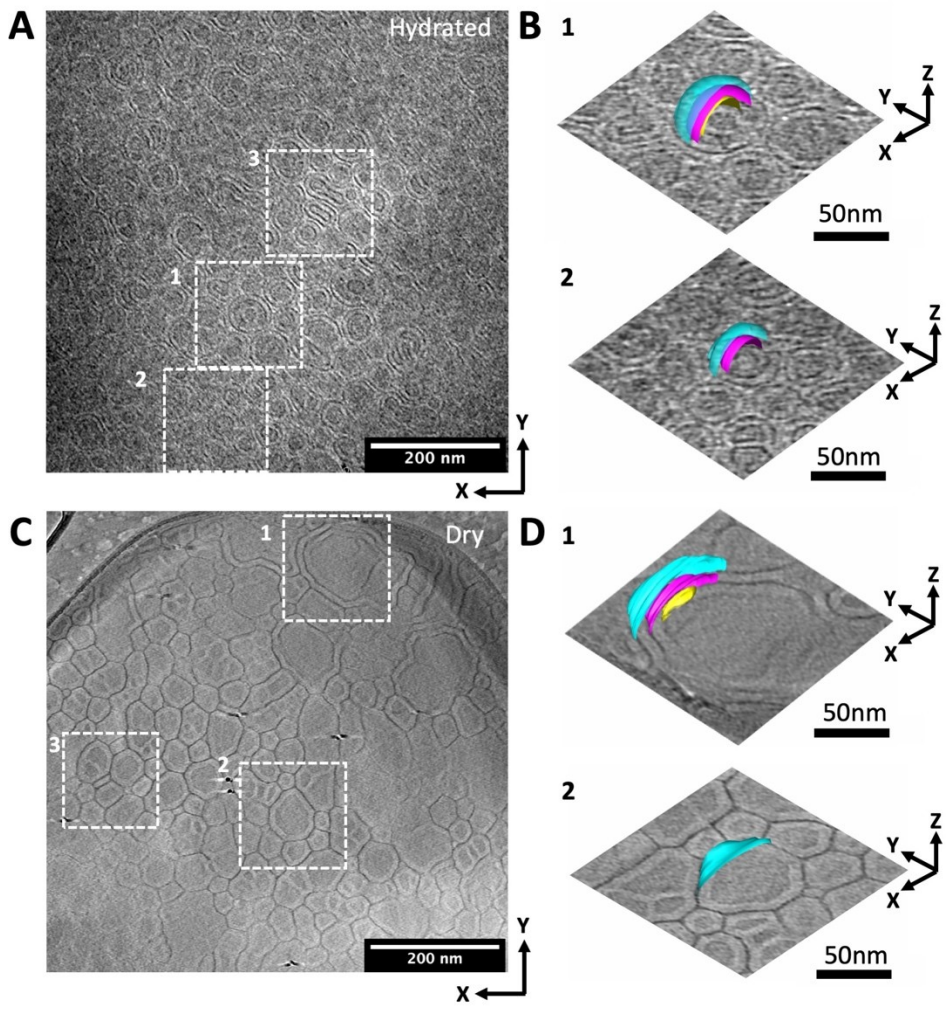

Figure 4. Slices in the tomograms show the morphological changes in the hydrated and dry $pNeh_{18}$-*b*-$pNpm_{18}$ thin films, respectively. **A**. a perpendicular slice through the tomogram of the hydrated $pNeh_{18}$-*b*-$pNpm_{18}$ thin film , **B.** 3D visualizations of two regions, 1 and 2, labeled by dashed boxes in A. **C**. a perpendicular slice through the tomogram of the dry $pNeh_{18}$-*b*-$pNpm_{18}$ thin film, **D.** 3D visualizations of two regions, 1 and 2, labeled by dashed boxes in C. Different colors represent the spatial distributions of the central regions of the electron dense (hydrophilic) pNpm blocks using mesh rendering in iMOD. The areas indicated by box 3 are shown in Figures 5 and 6. One slice along z direction is shown in each panel. The thickness of a slice is 0.8 nm.

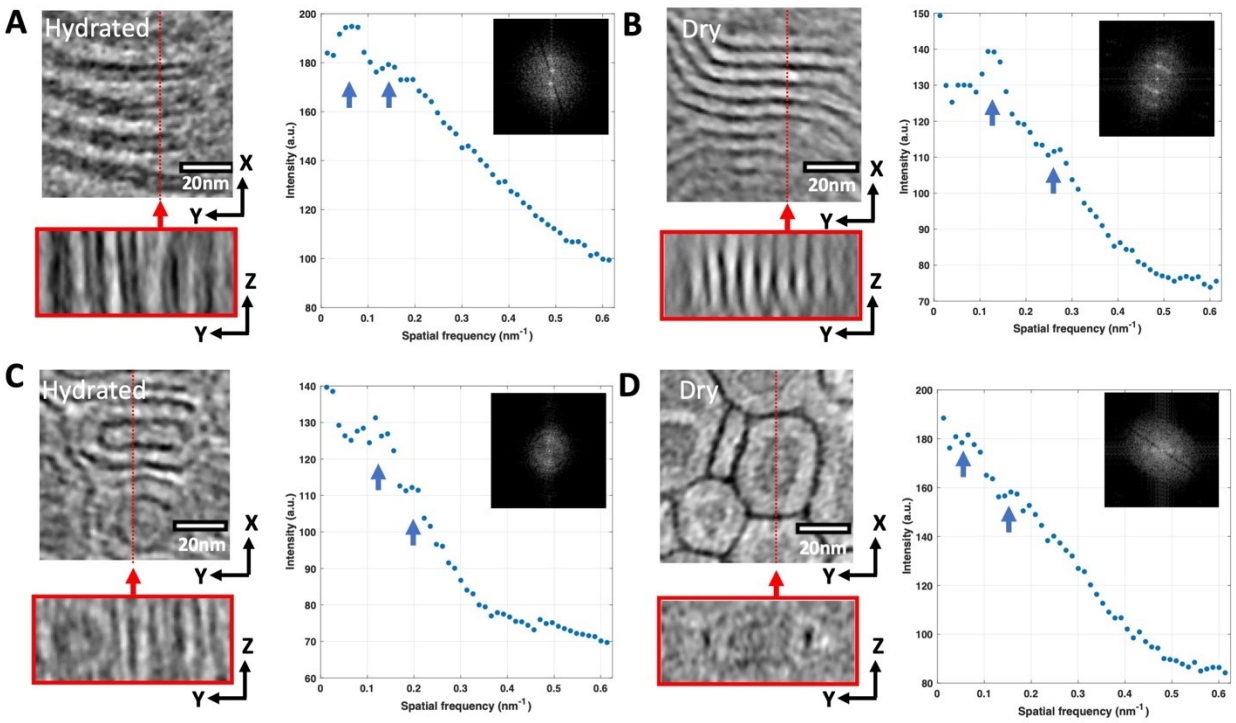

Figure 5. Small portions of slices in the tomograms show the morphological changes in the hydrated and the dry thin films. The dashed red lines represent the positions of the slices through *y*-*z* planes as shown at the bottom of each figure. The corresponding 2-D Fourier transforms (inset) and radially averaged 1-D FFT profiles are shown in the right panel as insets and plots, respectively. The arrows indicate the peaks in plots. **A and B.** Small portions of the perpendicular slices through the tomograms of the hydrated and dry $pNeh_9$-*b*-$pNpm_9$ thin film as indicated by the boxes 3 in Figures 3A and C. **C and D.** Small portions of the perpendicular slices through the tomograms of the hydrated and dry $pNeh_{18}$-*b*-$pNpm_{18}$ thin film as indicated by the boxes 3 in Figures 4A and C.

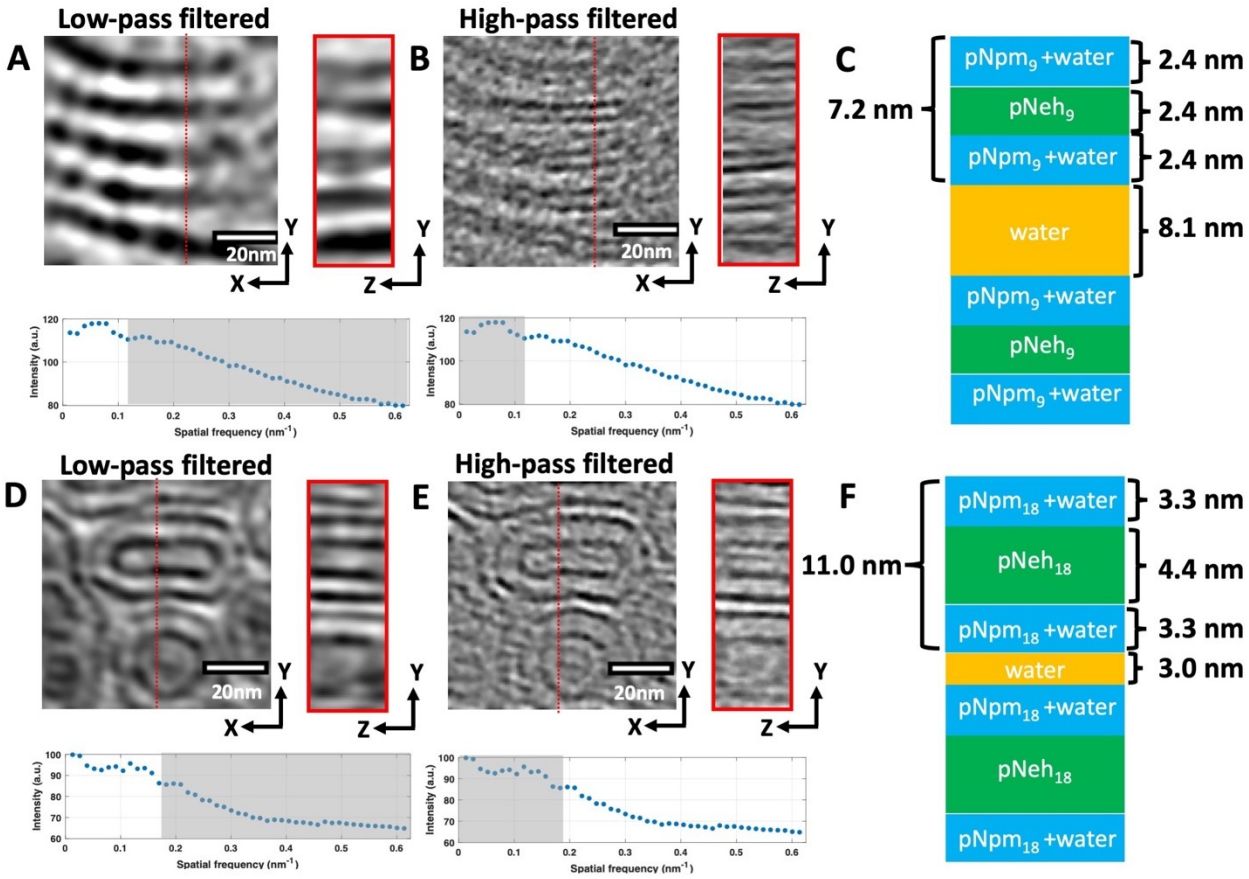

Figure 6. Spatial frequency filter with a cutoff frequency of 0.125 nm^{-1} and 0.166 nm^{-1} were applied to the slices of the hydrated $pNeh_9$-*b*-$pNpm_9$ film in Figure 5A and the hydrated $pNeh_{18}$-*b*-$pNpm_{18}$ film in Figure 5C, respectively. The actual frequency filters are shown in the 1-D FFT profiles at the bottom. Spatial frequency filtering enables the identification of the structures responsible for the different peaks in the 1-D FFT profiles. **A and B**, Low-pass and high-pass frequency filtered slices of the hydrated $pNeh_9$-*b*-$pNpm_9$ thin film. **D and E**, Low-pass and high-pass frequency filtered slices of the hydrated $pNeh_{18}$-*b*-$pNpm_{18}$ thin film. The dark regions represent the electron dense hydrophilic pNpm blocks. Schematic cartoons of the arrangement of domains in the hydrated $pNeh_9$-*b*-$pNpm_9$ and $pNeh_{18}$-*b*-$pNpm_{18}$ thin films are depicted in **C and F.**

Table 2. Summary of thickness measurements

Polypeptoids	Domain spacing Hydrated[1] (nm)	Domain spacing Dry[1] (nm)	Thin film thickness (hydrated/dry) (nm)	Hydrophobic pNeh domain size Hydrated/ Dry (nm)	Hydrophilic pNpm domain size Hydrated/Dry[2] (nm)	Water phase (nm)
$pNeh_9$-*b*-$pNpm_9$	7.2	7.5	240/130	2.4/4.2	4.8/3.3	8.1
$pNeh_{18}$-*b*-$pNpm_{18}$	11.0	10.5	100/30-70	4.4/7.0	6.6/3.5	3.0

[1.] Domain spacing is defined as the center to center distance between two electron dense domains in a cross-section profile in the dry samples. In the hydrated samples, domain spacing is defined as the thickness of the whole membrane, including two layers hydrophilic brushes and a hydrophobic core. The measurement method is reported in the previous study.[67]

[2.] Thickness of pNpm blocks in the hydrated film includes two layers of hydrophilic brushes.

References

[1] B. C. H. Steele, A. Heinzel. *Nature* **2001**, *414*, 345.
[2] Y. A. Elabd, M. A. Hickner. *Macromolecules* **2011**, *44*, 1.
[3] R. Bouchet, S. Maria, R. Meziane, A. Aboulaich, L. Lienafa, J. P. Bonnet, T. N. T. Phan, D. Bertin, D. Gigmes, D. Devaux, R. Denoyel, M. Armand. *Nat Mater* **2013**, *12*, 452.
[4] R. Yuan, A. A. Teran, I. Gurevitch, S. A. Mullin, N. S. Wanakule, N. P. Balsara. *Macromolecules* **2013**, *46*, 914.
[5] J. Haggin. *Chem Eng News* **1995**, *73*, 28.
[6] O. Onaca, R. Enea, D. W. Hughes, W. Meier. *Macromol Biosci* **2009**, *9*, 129.
[7] J. S. Lee, J. Feijen. *J Control Release* **2012**, *161*, 473.
[8] T. M. Allen, P. R. Cullis. *Adv Drug Deliver Rev* **2013**, *65*, 36.
[9] Z. X. Zhu, J. L. Anacker, S. X. Ji, T. R. Hoye, C. W. Macosko, R. K. Prud'homme. *Langmuir* **2007**, *23*, 10499.
[10] K. M. Pustulka, A. R. Wohl, H. S. Lee, A. R. Michel, J. Han, T. R. Hoye, A. V. McCormick, J. Panyam, C. W. Macosko. *Mol Pharmaceut* **2013**, *10*, 4367.
[11] S. J. Paddison. *Annu Rev Mater Res* **2003**, *33*, 289.
[12] J. Rivnay, S. Inal, B. A. Collins, M. Sessolo, E. Stavrinidou, X. Strakosas, C. Tassone, D. M. Delongchamp, G. G. Malliaras. *Nat Commun* **2016**, *7*.
[13] A. A. Pivovar, B. S. Pivovar. *J Phys Chem B* **2005**, *109*, 785.
[14] N. P. Blake, M. K. Petersen, G. A. Voth, H. Metiu. *J Phys Chem B* **2005**, *109*, 24244.
[15] K. Schmidt-Rohr, Q. Chen. *Nat Mater* **2008**, *7*, 75.
[16] S. N. Magonov, D. H. Reneker. *Annu Rev Mater Sci* **1997**, *27*, 175.
[17] G. H. Michler. Electron microscopy of polymers; Springer: Berlin, **2008**.
[18] D. T. Grubb. *J Mater Sci* **1974**, *9*, 1715.
[19] R. M. Glaeser, K. A. Taylor. *Journal of microscopy* **1978**, *112*, 127.
[20] R. F. Egerton, P. Li, M. Malac. *Micron* **2004**, *35*, 399.
[21] R. F. Egerton. *Ultramicroscopy* **2013**, *127*, 100.
[22] Z. J. W. A. Leijten, A. D. A. Keizer, G. de With, H. Friedrich. *J Phys Chem C* **2017**, *121*, 10552.
[23] Y. Y. Won, A. K. Brannan, H. T. Davis, F. S. Bates. *J Phys Chem B* **2002**, *106*, 3354.
[24] S. Jain, F. S. Bates. *Macromolecules* **2004**, *37*, 1511.
[25] E. P. Holowka, D. J. Pochan, T. J. Deming. *J Am Chem Soc* **2005**, *127*, 12423.
[26] E. Kesselman, Y. Talmon, J. Bang, S. Abbas, Z. B. Li, T. P. Lodge. *Macromolecules* **2005**, *38*, 6779.
[27] K. P. Davis, T. P. Lodge, F. S. Bates. *Macromolecules* **2008**, *41*, 8289.
[28] C. LoPresti, H. Lomas, M. Massignani, T. Smart, G. Battaglia. *J Mater Chem* **2009**, *19*, 3576.
[29] J. Lepault, F. Pattus, N. Martin. *Biochim Biophys Acta* **1985**, *820*, 315.
[30] Y. Tahara, Y. Fujiyoshi. *Micron* **1994**, *25*, 141.
[31] G. Gebel. *Polymer* **2000**, *41*, 5829.
[32] L. Rubatat, O. Diat. *Macromolecules* **2007**, *40*, 9455.
[33] C. Wang, S. J. Paddison. *Soft Matter* **2014**, *10*, 819.

[34] P. J. James, J. A. Elliott, T. J. McMaster, J. M. Newton, A. M. S. Elliott, S. Hanna, M. J. Miles. *J Mater Sci* **2000**, *35*, 5111.
[35] M. Bass, A. Berman, A. Singh, O. Konovalov, V. Freger. *J Phys Chem B* **2010**, *114*, 3784.
[36] J. Wu, X. H. Zhu, M. M. West, T. Tyliszczak, H. W. Shiu, D. Shapiro, V. Berejnov, D. Susac, J. Stumper, A. P. Hitchcock. *J Phys Chem C* **2018**, *122*, 11709.
[37] S. Yakovlev, K. H. Downing. *Phys Chem Chem Phys* **2013**, *15*, 1052.
[38] M. A. Modestino, D. K. Paul, S. Dishari, S. A. Petrina, F. I. Allen, M. A. Hickner, K. Karan, R. A. Segalman, A. Z. Weber. *Macromolecules* **2013**, *46*, 867.
[39] G. S. Hwang, D. Y. Parkinson, A. Kusoglu, A. A. MacDowell, A. Z. Weber. *Acs Macro Lett* **2013**, *2*, 288.
[40] J. P. James, H. W. Choi, J. G. Pharoah. *Int J Hydrogen Energ* **2012**, *37*, 18216.
[41] M. Maier, J. Dodwell, R. Ziesche, C. Tan, T. Heenan, J. Majasan, N. Kardjilov, H. Markotter, I. Manke, L. Castanheira, G. Hinds, P. R. Shearing, D. J. L. Brett. *J Power Sources* **2020**, *455*.
[42] H. Uchida, J. M. Song, S. Suzuki, E. Nakazawa, N. Baba, M. Watanabe. *J Phys Chem B* **2006**, *110*, 13319.
[43] S. V. Venkatesan, M. El Hannach, S. Holdcroft, E. Kjeang. *J. Membr. Sci.* **2017**, *539*, 138.
[44] F. I. Allen, L. R. Comolli, A. Kusoglu, M. A. Modestino, A. M. Minor, A. Z. Weber. *Acs Macro Lett* **2015**, *4*, 1.
[45] C. J. Newcomb, T. J. Moyer, S. S. Lee, S. I. Stupp. *Curr Opin Colloid In* **2012**, *17*, 350.
[46] N. M. Benetatos, C. D. Chan, K. I. Winey. *Macromolecules* **2007**, *40*, 1081.
[47] D. L. Handlin, E. L. Thomas, W. J. Macknight. *Macromolecules* **1981**, *14*, 795.
[48] S. Takahashi, J. Shimanuki, T. Mashio, A. Ohma, H. Tohma, A. Ishihara, Y. Ito, Y. Nishino, A. Miyazawa. *Electrochim Acta* **2017**, *224*, 178.
[49] C. Li, R. A. Register, S. L. Cooper. *Polymer* **1989**, *30*, 1227.
[50] B. P. Grady. *Polym Eng Sci* **2008**, *48*, 1029.
[51] A. Singh, A. G. Kumar, S. Saha, R. Mukherjee, S. Bisoi, S. Banerjee. *Polym Eng Sci* **2019**, *59*, 2279.
[52] J. Wang, X. J. Wang, P. Dou, H. Zhang, Y. M. Zhang. *Polym Eng Sci* **2015**, *55*, 180.
[53] S. Yakovlev, N. P. Balsara, K. H. Downing. *Membranes* **2013**, *3*, 424.
[54] S. Yakovlev, X. Wang, P. Ercius, N. P. Balsara, K. H. Downing. *J Am Chem Soc* **2011**, *133*, 20700.
[55] B. E. McKenzie, S. J. Holder, N. A. J. M. Sommerdijk. *Curr Opin Colloid In* **2012**, *17*, 343.
[56] J. P. Patterson, Y. F. Xu, M. A. Moradi, N. A. J. M. Sommerdijk, H. Friedrich. *Accounts Chem Res* **2017**, *50*, 1495.
[57] P. M. Frederik, N. Sommerdijk. *Curr Opin Colloid In* **2005**, *10*, 245.
[58] A. L. Parry, P. H. H. Bomans, S. J. Holder, N. A. J. M. Sommerdijk, S. C. G. Biagini. *Angew Chem Int Edit* **2008**, *47*, 8859.
[59] X. C. Chen, X. Jiang, N. P. Balsara. *J Chem Phys* **2018**, *149*.
[60] M. Rikukawa, K. Sanui. *Prog Polym Sci* **2000**, *25*, 1463.
[61] A. L. Rusanov, P. V. Kostoglodov, M. J. M. Abadie, V. Y. Voytekunas, D. Y. Likhachev. *Adv Polym Sci* **2008**, *216*, 125.
[62] J. Sun, X. Jiang, A. Siegmund, M. D. Connolly, K. H. Downing, N. P. Balsara, R. N. Zuckermann. *Macromolecules* **2016**, *49*, 3083.

[63] S. Q. Zheng, E. Palovcak, J. P. Armache, K. A. Verba, Y. F. Cheng, D. A. Agard. *Nat Methods* **2017**, *14*, 331.
[64] J. R. Kremer, D. N. Mastronarde, J. R. McIntosh. *Journal of structural biology* **1996**, *116*, 71.
[65] T. D. Gierke, G. E. Munn, F. C. Wilson. *J Polym Sci Pol Phys* **1981**, *19*, 1687.
[66] B. Loppinet, G. Gebel. *Langmuir* **1998**, *14*, 1977.
[67] X. Jiang, R. K. Spencer, J. Sun, C. Ophus, R. N. Zuckermann, K. H. Downing, N. P. Balsara. *J Phys Chem B* **2019**, *123*, 1195.
[68] Y. Cohen, R. J. Albalak, B. J. Dair, M. S. Capel, E. L. Thomas. *Macromolecules* **2000**, *33*, 6502.
[69] L. Zhu, S. Z. D. Cheng, B. H. Calhoun, Q. Ge, R. P. Quirk, E. L. Thomas, B. S. Hsiao, F. Yeh, B. Lotz. *Polymer* **2001**, *42*, 5829.
[70] P. Mueller, T. F. Chien, B. Rudy. *Biophys J* **1983**, *44*, 375.
[71] M. I. Angelova, S. Soléau, P. Méléard, F. Faucon, P. Bothorel. Darmstadt, 1992, pp 127.
[72] S. Jang, S. Y. Kim, H. Y. Jung, M. J. Park. *Macromolecules* **2018**, *51*, 1120.
[73] H. Y. Jung, O. Kim, M. J. Park. *Macromolecular rapid communications* **2016**, *37*, 1116.
[74] X. C. Chen, D. T. Wong, S. Yakovlev, K. M. Beers, K. H. Downing, N. P. Balsara. *Nano Lett* **2014**, *14*, 4058.
[75] D. R. Greer, M. A. Stolberg, J. Kundu, R. K. Spencer, T. Pascal, D. Prendergast, N. P. Balsara, R. N. Zuckermann. *J Am Chem Soc* **2018**, *140*, 827.
[76] D. R. Greer, M. A. Stolberg, S. T. Xuan, X. Jiang, N. P. Balsara, R. N. Zuckermann. *Macromolecules* **2018**, *51*, 9519.
[77] S. Koizumi, H. Hasegawa, T. Hashimoto. *Makromol Chem-M Symp* **1992**, *62*, 75.

Graphical abstract